A Letters Journal Exploring the Frontiers of Physics

December 2019

EPL, **128** (2019) 60001
doi: 10.1209/0295-5075/128/60001

www.epljournal.org

Detecting structured sources in noisy images via Minkowski maps

Michael A. Klatt[1] and Klaus Mecke[2]

[1] *Department of Physics, Princeton University - Princeton, NJ 08544, USA*
[2] *Institut für Theoretische Physik, FAU Erlangen-Nürnberg - Staudtstr. 7, 91058 Erlangen, Germany*

received 13 September 2019; accepted in final form 21 December 2019
published online 31 January 2020

PACS 07.05.Kf – Data analysis: algorithms and implementation; data management
PACS 02.50.-r – Probability theory, stochastic processes, and statistics
PACS 02.40.-k – Geometry, differential geometry, and topology

Abstract – Astronomy, biophysics, and material science often depend on the possibility to extract information out of faint spatial signals. Here we present a morphometric analysis technique to quantify the shape of structural deviations in greyscale images. It identifies important features in noisy spatial data, especially for short observation times and low statistics. Without assuming any prior knowledge about potential sources, the additional shape information can increase the sensitivity by 14 orders of magnitude compared to previous methods. Rejection rates can increase by an order of magnitude. As a key ingredient to such a dramatic increase, we accurately describe the distribution of the homogeneous background noise in terms of the density of states $\Omega(A, P, \chi)$ for the area A, perimeter P, and Euler characteristic χ of random black-and-white images. The technique is successfully applied to data of the H.E.S.S. experiment for the detection of faint extended sources.

Distinguishing a feature from background noise is often the key to discovering physical phenomena in spatial data, from detecting sources in gamma-ray astronomy [1–5] to tumor recognition in medical imaging [6–8], and from geospatial sensing in earth science to a broad spectrum of video analyses and pattern recognition [9,10]. In particular, for short observation times and low statistics, when faint extended signals are overlaid by strong background noise, a sensitive analysis is required that comprehensively and robustly characterizes the features in the observed gray-scale images.

It is well established that Minkowski functionals from integral geometry comprehensively and robustly quantify the complex shape that arises in spatial data [10–15]. For example, they have been successfully applied in astronomy and cosmology [16–25], material science of heterogeneous and porous media [26], random or rough surfaces [27,28], complex fluids [29], biology [30,31], and medical physics [32,33]. In 2D, the Minkowski functionals are the area A, perimeter P, and Euler characteristic χ. The latter is a topological constant that is given by the number of clusters minus the number of holes; for more details, see the Supplementary Material (`Supplementarymaterial.pdf` (SM)).

Here, we utilize the Minkowski functionals for a sensitive hypothesis test of gray-scale images. We present a morphometric analysis technique based on a geometric shape characterization that can increase the sensitivity by up to 14 orders of magnitude compared to previous methods [5]. While common null hypothesis tests do not use geometric information [1], full likelihood fits of models to measured data [2,4] strongly depend on the model and *a priori* knowledge about the sources. We demonstrate how —without prior assumptions about potential sources— a refined structural quantification of the spatial data and its deviation from the background can dramatically improve the detection of structural features in noisy greyscale images.

Our null hypothesis is that there are only background signals, which are randomly, independently, and homogeneously distributed over the field of view, and that therefore the number of events in each pixel (the counts) is an independent Poisson random number. Detector effects like nonuniform exposure that distort the homogeneous and isotropic background can efficiently be corrected as we demonstrate in the SM and in the analysis of an experimental sky map below. Even if the background model differs more fundamentally and includes correlations between pixels, our test can be generalized. It then requires sufficiently precise empirical distributions (for which the additivity of the Minkowski functionals is an advantage).

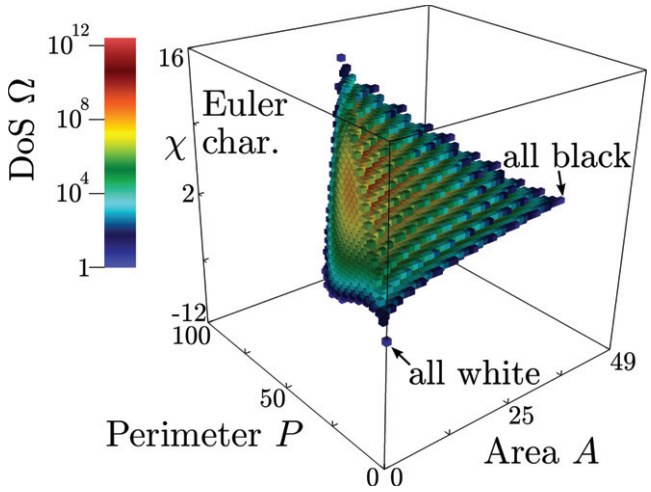

Fig. 1: Density of states Ω (DoS) for 7 × 7 pixels: each small cube represents a possible value of area A, perimeter P, and Euler characteristic χ (macrostate). Its color indicates the corresponding number of b/w images (microstates). For visualizations of up to 15 × 15 pixels, see the SM.

The first and most important ingredient of our analysis is the structure quantification by Minkowski functionals. To this end, the original image is converted into a black-and-white (b/w) image by thresholding (that is, all pixels with a greyscale larger than or equal to a given threshold ρ are set to black, otherwise they are set to white). The Minkowski functionals are then evaluated for the union of black pixels; for more details, see the Methods section.

The second crucial step is to compute the joint probability distribution $\mathcal{P}(A, P, \chi)$ of the Minkowski functionals under the assumption of the null hypothesis. An accurate estimate of $\mathcal{P}(A, P, \chi)$ provides detailed knowledge about the background structure, which in turn allows for a sensitive source detection. As explained below, we achieve such a precise estimate by combining the Wang-Landau algorithm from statistical physics [34] with analytic results about the "density of states" (DoS), see fig. 1, where the DoS $\Omega(A, P, \chi)$ is the number of b/w images with the same Minkowski functionals A , P, and χ. The probability $\mathcal{P}(A, P, \chi)$ to find a configuration with area A, perimeter P and Euler characteristic χ is then given by

$$\mathcal{P}(A, P, \chi) = \Omega(A, P, \chi) p_\rho^A (1 - p_\rho)^{N^2 - A}, \qquad (1)$$

where p_ρ is the probability that a pixel is black at a given threshold ρ. Since the distribution is derived for a pixelated image, there are no pixelization errors. The normalization of $\mathcal{P}(A, P, \chi)$ in eq. (1) follows from $\sum_{P,\chi} \Omega(A, P, \chi) = \binom{N^2}{A}$, that is, the number of configurations where A out of N^2 pixels are black is given by the binomial coefficient. Hence, for all values of ρ and N, we obtain $\sum_{A,P,\chi} \mathcal{P}(A, P, \chi) = \sum_A p_\rho^A (1 - p_\rho)^{N^2 - A} \sum_{P,\chi} \Omega(A, P, \chi) = \sum_A \binom{N^2}{A} p_\rho^A (1 - p_\rho)^{N^2 - A} = 1$. Notably, if we do not distinguish states by their perimeter and Euler characteristic, the probability mass function of the area A is binomial: $\mathcal{P}(A) = \sum_{P,\chi} \mathcal{P}(A, P, \chi) = \binom{N^2}{A} p_\rho^A (1 - p_\rho)^{N^2 - A}$.

The central idea of the morphometric analysis is to identify structures via significant deviations from the background noise. Similar to a likelihood ratio with no constraints on alternative hypotheses [5], we define the *compatibility* $\mathcal{C}$ of a measured triplet (A, P, χ) with the null hypothesis by

$$\mathcal{C}(A, P, \chi) := \sum_{\mathcal{P}(A_i, P_i, \chi_i) \le \mathcal{P}(A, P, \chi)} \mathcal{P}(A_i, P_i, \chi_i). \qquad (2)$$

It is the probability for the appearance of a structure in the background that is as likely as or less likely than the measured structure. For an intuitive measure that gets larger if the structural deviation is stronger, we define the *deviation strength* $\mathcal{D}$ as the negative logarithm of the compatibility:

$$\mathcal{D}(A, P, \chi) := -\log_{10} \mathcal{C}(A, P, \chi). \qquad (3)$$

The compatibility or deviation strength can be used as a test statistic in a null hypothesis test. Below, we reject the assumption of pure background signals if the compatibility is lower than 0.6×10^{-6} or equivalently if the deviation strength is larger than 6.2. We have picked these critical values in analogy to the commonly used 5σ deviation for a normally distributed random variable.

The third ingredient of our morphometric analysis is to analyze the image not globally but locally in small scan windows W_N of size $N \times N$, where the W_N are still large enough to contain structural features (typically $16 > N > 4$). Assigning the maximum value of the deviation strength for all thresholds to the central pixel of W_N, we obtain a *Minkowski map* of the gray-scale data, see fig. 2. For hypothesis tests, a conservative estimator of the trial factor can take the repeated trials at different thresholds and positions of W_N into account [5] similar to "significance maps" in gamma-ray astronomy [35]. Minkowski maps have been used already in gamma-ray astronomy [5] but only based on the area A.

To compare this simple structure characterization to our new joint characterization with all Minkowski functionals, we simulate a test pattern with sources of different sizes and intensities, shown in fig. 2(a); for more details, see the Methods section. The image is first analyzed by a Minkowski sky map based on the *simple* deviation strength $\mathcal{D}(A)$, which uses only the area A, see fig. 2(b). Then we compute the Minkowski sky map based on the *joint* deviation strength $\mathcal{D}(A, P, \chi)$, which uses the three Minkowski functionals, see fig. 2(c). By analyzing the same data with all Minkowski functionals instead of only the area, the compatibility with the background structure decreases by orders of magnitude. Sources that were hardly visible before can now be clearly detected.

For a systematic analysis, we simulate a bell-shaped source (at various intensities), see fig. 3; for more

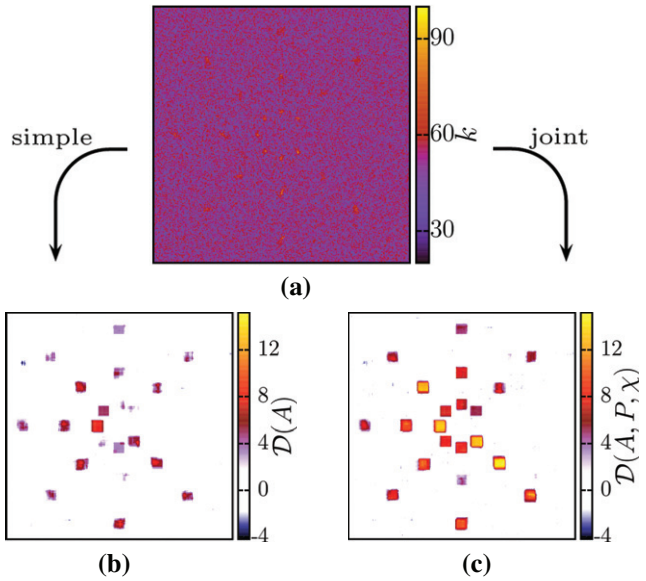

Fig. 2: Strong increase in sensitivity via joint structure characterization: (a) simulated counts map that includes sources of different sizes and different integrated fluxes. It is analyzed by two Minkowski sky maps: based on (b) the simple deviation strength $\mathcal{D}(A)$, which uses only the area, and (c) the joint deviation strength $\mathcal{D}(A, P, \chi)$, which uses all Minkowski functionals. The latter makes it possible to detect all sources.

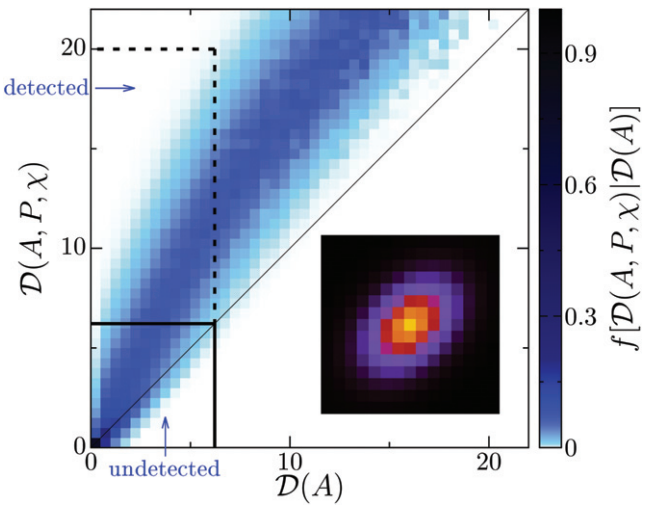

Fig. 3: Systematic analysis of a dramatic increase in sensitivity: it compares the simple and joint deviation strengths for the bell-shaped source profile shown in the inset. Given $\mathcal{D}(A)$, the color shows the frequency f of $\mathcal{D}(A, P, \chi)$ for the same data. The analysis based on $\mathcal{D}(A, P, \chi)$ is distinctly more sensitive for the given source (inset) with a nontrivial shape, that is, with a strong intensity gradient in the scan window.

details, see the Methods section. Given a simple deviation strength $\mathcal{D}(A)$, we estimate the conditional frequency $f[\mathcal{D}(A, P, \chi)|\mathcal{D}(A)]$ of the joint deviation strength $\mathcal{D}(A, P, \chi)$. More precisely, we compute for all bins with a given value of $\mathcal{D}(A)$ the empirical probability density function of $\mathcal{D}(A, P, \chi)$. Figure 3 shows that the joint $\mathcal{D}(A, P, \chi)$ is for the source profile shown in the inset most often dramatically larger than the simple $\mathcal{D}(A)$. For samples for which the simple deviation strength based only on the area is below 5, that is, for which the compatibility is greater than 10^{-5}, the joint deviation strength sometimes exceeds 19, which corresponds to a compatibility less than 10^{-19}. If the structure is characterized not only by the area but by all Minkowski functionals, the compatibility with the background structure can drop by up to 14 orders of magnitude.

Simply by taking additional morphometric information into account, a formerly undetected source is now eventually detected in the same data. The vertical and horizontal solid lines in fig. 3 indicate the critical value of the null hypothesis test defined above. For all images for which the corresponding values of the deviation strengths are within the dashed box, the source is not detected if only the area characterizes the structure, but the null hypothesis is rejected using the joint deviation strength, that is, if all Minkowski functionals characterize the shape of the image.

The rate of rejections, that is, the percentage of samples for which the null hypothesis is rejected, depends on the intensity of the source, that is, the expected number of source signals, and on the background intensity. For a broad range of source intensities, table 1 reports the empirical rejection rates of the null hypothesis tests based on either $\mathcal{D}(A)$ or $\mathcal{D}(A, P, \chi)$. Both analyze the same samples from fig. 3, and in both cases the null hypothesis is rejected if the test statistic is larger than 6.2, which corresponds to a significance level of 0.6×10^{-6}. If there are, for example, on average, 576 source signals among 22500 background events, the rejection rate using $\mathcal{D}(A)$ is 5.6%. Using $\mathcal{D}(A, P, \chi)$, *i.e.*, all Minkowski functionals, the rejection rate rises by almost an order of magnitude to 53%.

Whether our morphometric analysis indeed detects a formerly undetected source depends, of course, on its shape. An increase in sensitivity can only be achieved if there is nontrivial shape information within the scan window W_N, more precisely, if the shape of the source is properly structured on the scale of W_N.

This intuition can be more formally explained with the help of fig. 4. It depicts the joint probability density function of area A and perimeter P assuming only background signals. Given a measured area, say $A = 128$, the compatibility $\mathcal{C}(A)$ sums the probabilities for areas that are less or equally likely than the measured value, in this case, areas larger than 127 or smaller than 98 (indicated by the two vertical lines in fig. 4). For the joint compatibility $\mathcal{C}(A, P)$, we consider two cases: $P = 242$ (green square) and $P = 218$ (blue square). The first value is very likely to occur if there is, for example, a uniform offset in the intensity. The corresponding compatibility is the sum over all probabilities outside the inner contour line so that $\mathcal{C}(A, P) > \mathcal{C}(A)$. However, in the presence of a structured source, the perimeter P might take on a value that

Table 1: Rejection rates for the simulated sources from fig. 3, comparing the null hypothesis tests based on either only the area (second column) or all Minkowski functionals (third column). The level of significance is 0.6×10^{-6} for all tests. The mean number of background events per sample is 22500. The average number of source signals (first column) varies from weak to bright sources. For each value, the rejection rate impressively improves if all Minkowski functionals are included in the analysis.

Avg. #source signals	Rejection rates	
	$\mathcal{D}(A)$	$\mathcal{D}(A,P,\chi)$
384	0.098%	2.1%
432	0.28%	6.6%
480	0.79%	16%
528	2.3%	33%
576	5.6%	53%
624	12%	73%
672	24%	88%
720	40%	96%
768	59%	99%

is unlikely in the background model, like $P = 218$. In this second case, the compatibility $\mathcal{C}(A,P)$ is the sum over all probabilities outside the outer contour line, which results in $\mathcal{C}(A,P) < \mathcal{C}(A)$. A structural deviation from the background thus leads to a smaller compatibility with the null hypothesis. Two b/w images that seem to have the same compatibility with the background if measured by only the area can be clearly distinguished using the additional information of the perimeter.

Strong inhomogeneities may thus be detected even if there is no excess in the total number of counts. Our method should, therefore, be robust against overestimated background intensities and should depend less on the choice of the size N of the window than methods based only on the total number of counts like in ref. [1]. There is no general comparison that universally favors one of these statistical methods. The advantages strongly depend on experimental details and the data, like the shape of sources as explained above. For instance, in gamma-ray astronomy: if there are no distinctive features within the scan window, a standard counting method [1] is more likely to detect sources than our morphometric analysis since the shape information yields no advantage over a specialization on the total number of counts. On the other hand, if the Minkowski functionals capture a significant structural difference from the background noise, our morphometric analysis may detect a source even if the total number of counts is insignificant.

The computationally most expensive step in the preparation of the morphometric analysis was, as indicated in the introduction, to determine the DoS $\Omega(A,P,\chi)$ in eq. (1). For small observation windows (up to 6×6), we directly computed the Minkowski functionals for all

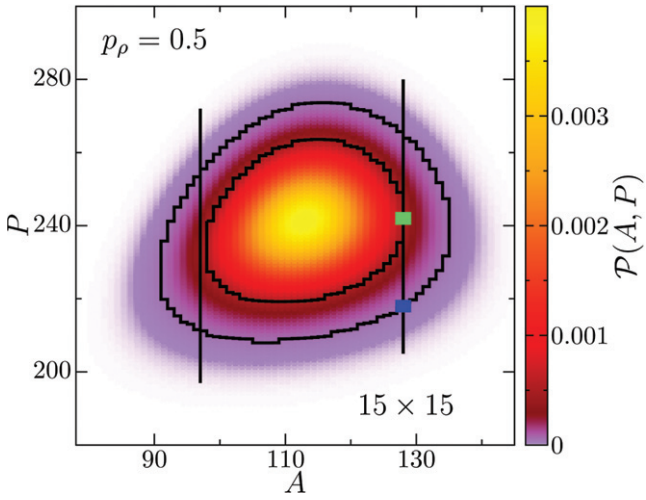

Fig. 4: Probability distribution $\mathcal{P}$ of area A and perimeter P of a b/w image with 15×15 pixels for a probability $p_\rho = 0.5$ that a pixel is black.

possible b/w images. For larger windows like 15×15, the DoS can no longer be determined analytically but has to be estimated numerically. The challenge is that a simple sampling of the space of microstates (estimating the DoS by the frequency of macrostates) cannot provide reliable estimates of the DoS for both values of $\mathcal{O}(10^{64})$ and $\mathcal{O}(1)$. However, configurations corresponding to the latter may be likely to appear if there is a source in the observation window. Therefore we apply the so-called Wang-Landau algorithm, which was developed in statistical physics to study phase transitions and critical phenomena [34,36].

Even this would not suffice (for 15×15 pixels) if we straightforwardly used the triple of Minkowski functionals, A, P, and χ, as "energy". Such a standard implementation that inverts the color of a randomly chosen pixel is too inefficient since there are millions of potential macrostates. Instead, we fix the number of black pixels (*i.e.*, the area A) since we analytically know the number of these configurations to be $\binom{N^2}{A}$. At each step of the random walk through the space of microstates, we randomly exchange a black and a white pixel. By splitting the space of macrostates into disjoint subsets, we only have to estimate the DoS with respect to P and χ and thus reduce the number of potential macrostates in a 15×15 scan window to about 10^4. Each simulation can be independently completed within three days on a single-core. Another advantage of our combination of numerical estimates and analytic knowledge is that it guarantees that $\mathcal{P}(A,P,\chi)$ is exactly normalized as explained above. Moreover, we can analytically determine the DoS for small or large values of A, which is important for point-like sources resulting in only a few black pixels at high thresholds.

Figure 1 visualizes the DoS for a 7×7 Poisson random field of pixels, see also fig. 1 in the SM and Supplementary Animations 1 (`Animation1.gif`) and 2 (`Animation2.txt`). Each small cube represents a

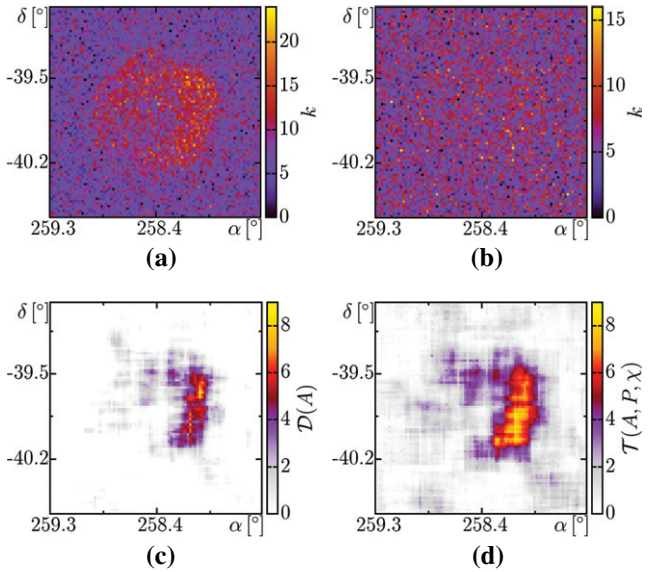

Fig. 5: Sky maps of RX J1713.7–3946: (a) H.E.S.S. counts map with a clearly visible source [3,5], (b) source signals are suppressed by postselection and Monte Carlo noise that is added to the counts map, (c) the former test statistic $\mathcal{D}(A)$ applied to (b) hints towards a source. The refined analysis based on $\mathcal{T}(A, P, \chi)$ in (d) strongly increases the sensitivity, so that the source is clearly detected.

macrostate and its color the corresponding DoS. Complex features, like discrete steps between neighboring macrostates, are not artifacts but appear due to the finite system size. Interestingly, for growing window sizes, the DoS appears to converge quickly to an asymptotic distribution [37], which could make it possible to estimate the joint deviation strength of even larger observation windows.

If we combine the deviation strengths at different thresholds, we can further improve the sensitivity of our analysis for diffuse radiation or very extended sources. The maximum of the deviation strengths for all thresholds can, for example, be replaced by the sum of $\mathcal{D}(A, P, \chi)$. Based on 10^9 simulated samples, we determine its empirical complementary cumulative distribution function (ECCDF). Given a measured sum of deviation strengths, the ECCDF estimates the probability to find a larger value. Its negative decadic logarithm serves as a new test statistic $\mathcal{T}(A, P, \chi)$ analogous to $\mathcal{D}(A, P, \chi)$.

We apply this technique to experimental data of a supernova remnant, the gamma-ray source RX J1713.7−3946, as observed by the H.E.S.S. experiment, a ground-based gamma-ray telescope. The data set used here is the same as in ref. [5], which in turn was based on the data in ref. [3]. It is an extended source, see fig. 5(a), whose shape has already been studied in detail [3]. An increase in sensitivity of such a well-observed and highly significant source is not necessary. So we use it as a benchmark data set but artificially reduce the sensitivity by first reducing the number of counts via Monte Carlo postselection (keeping on average only 11% of the data) and then adding Monte Carlo observations of background noise [5,38]. In the resulting counts map in fig. 5(b), the source is hardly visible by eye.

Figures 5(c) and 5(d) compare the deviation strength $\mathcal{D}(A)$, which only uses the area and thus the number of counts, to our new test statistic $\mathcal{T}(A, P, \chi)$. As described above, the latter combines the deviation strengths at different thresholds and simultaneously characterizes the shape of the counts map by all three Minkowski functionals. This clearly leads to a strong increase in sensitivity even in the logarithmic scales of $\mathcal{D}(A)$ and $\mathcal{T}(A, P, \chi)$. Moreover, the original shape of the supernova remnant is better visible.

In summary, our morphometric analysis of gray-scale images detects features via structural deviations from the background noise. Its main advantage is that by combining all Minkowski functionals, sensitive structure information is taken into account without requiring any prior knowledge about potential sources. Our Minkowski maps can detect inhomogeneities in images even when there is no excess in the total number of counts. This is especially important for low intensities, where fluctuations in the total number of counts are often not statistically significant, but a source can be detected via the clustering of black pixels. The comprehensive Minkowski functionals include all additive —and therefore robust— geometrical information [11]. The additivity and thus linear scaling of the computation time makes it possible to efficiently analyze large data sets.

Importantly, going beyond the sensitive analysis of gamma-ray sky maps, we here propose a versatile morphometric analysis of a broad spectrum of gray-scale images with promising applications from medicine to soft matter physics. In statistics, we have designed —parallel to this study— a family of test statistics based on Minkowski functionals and their empirical distributions. They can be used in a morphometric hypothesis test for the complete spatial randomness of point patterns [37]. Promising prospects of future research are to explore further connections to related and complementary techniques in the spatial statistics of point processes [39–41], astronomy, and cosmology [16–18,21–23], to combine their distinct advantages, and to tailor the analysis to the requirements of applications, like an unknown background intensity. A fascinating open question is whether our refined shape analysis leads for correlated models to a similarly strong or even stronger increase in sensitivity.

Methods. – The Minkowski functionals are calculated for the unions of black pixels. We do so by summing the contributions of 2×2 neighborhoods using the look-up table from ref. [5]. The area of a single black pixel is one, its perimeter four. To more easily detect clusters of black pixels, we choose to connect pixels that touch at one corner.

Because our model is discrete and directly defined on the (square) lattice, there is no pixelation error or bias in

our analysis. Importantly, we compute the probability distribution of the Minkowski functionals consistently (that is, for a discrete random field).

Only for a generalization to other models that require a comparison to smooth random fields, pixelation effects would need to be corrected. In that case, the connectivity of black pixels that touch at a corner should be redefined to avoid a bias in the Euler characteristic. A convenient solution is to assign zero contribution to such configurations, which corresponds to the mean value if the pixels are connected or disconnected with equal probability [19,20]. Bias-free estimators of all Minkowski functionals (and tensors) can also be defined using a marching square algorithm based on the original gray values (before thresholding) [10]. Such gray-value–based estimators are bias-free in the limit of infinite resolution (under weak conditions) [42]. Another bias-free estimator is based on Voronoi tessellations [43].

Our hypothesis test can be defined for any boundary condition [14]. It is only important that the choice is consistent for the probability distribution and measured data. Here, we choose closed boundary conditions, which means that the exterior of the observation window is chosen to be white. Thus, the three functionals access the same information, which guarantees that our reported sensitivity increase is solely due to an improved structure characterization. In contrast, minus sampling boundary conditions use real data to define the boundary. Thus, the perimeter and Euler characteristic access more data than the area. It can lead to an additional increase in sensitivity —a potential advantage that can be explored in future work.

We simulate the counts maps for figs. 2 and 3 by independently sampling the number of counts for each pixel from a Poisson random variable. The mean value is the sum of the expected number of background signals and the mean number of source signals within this pixel.

In fig. 2, the background intensity is 50. The test pattern includes 21 sources with different intensities (increasing counter-clockwise) and broadness (expanding outwardly). The profiles of the sources are Gaussian. The total number of expected source signals varies from about 350 to 550. The size of the sliding observation window for the Minkowski sky map is 15×15.

In fig. 3, we use a fixed source profile within 15×15 pixels (shown in the inset) and a background intensity of 100. We then vary the expected total number of source signals in 75 steps from 6 to 888. For each value, we simulate 100000 samples. For each sample, we determine $\mathcal{D}(A)$ and $\mathcal{D}(A, P, \chi)$. The final estimate of the conditional frequency $f[\mathcal{D}(A, P, \chi)|\mathcal{D}(A)]$ is an average over 100 estimates, each derived from 1000 independent samples.

The density of states and our code for Minkowski maps are available at the GitHub repository [44]. All simulated data and parameters underlying this study are available at the Zenodo repository [45]. H.E.S.S. observations of RX J1713.7−3946 (archival data) are publicly available [46].

* * *

We thank Christian Stegmann and Daniel Göring for valuable discussions and suggestions; we are grateful for their advice and expertise on gamma-ray astronomy. We thank the H.E.S.S. Collaboration for kindly providing data from their experiment. We thank the German Research Foundation (DFG) for the Grants No. ME1361/11, HU1874/3-2, and LA965/6-2 awarded as part of the DFG-Forschergruppe FOR 1548 "Geometry and Physics of Spatial Random Systems."

REFERENCES

[1] Li T.-P. and Ma Y.-Q., *Astrophys. J.*, **272** (1983) 317.
[2] Mattox J. R. *et al.*, *Astrophys. J.*, **461** (1996) 396.
[3] Aharonian F. *et al.*, *Astron. Astrophys.*, **449** (2006) 223.
[4] Atwood W. B. *et al.*, *Astrophys. J.*, **697** (2009) 1071.
[5] Göring D., Klatt M. A., Stegmann C. and Mecke K., *Astron. Astrophys.*, **555** (2013) A38.
[6] Canuto H. C. *et al.*, *Magn. Reson. Med.*, **61** (2009) 1218.
[7] Larkin T. J. *et al.*, *Magn. Reson. Med.*, **71** (2014) 402.
[8] Michel T. *et al.*, *Phys. Med. Biol.*, **58** (2013) 2713.
[9] Jain A. K., Duin R. P. W. and Mao J., *IEEE Trans. Pattern Anal.*, **22** (2000) 4.
[10] Mantz H., Jacobs K. and Mecke K., *J. Stat. Mech.*, **12** (2008) P12015.
[11] Schneider R. and Weil W., *Stochastic and Integral Geometry (Probability and Its Applications)* (Springer, Berlin) 2008.
[12] Schröder-Turk G. E., Kapfer S., Breidenbach B., Beisbart C. and Mecke K., *J. Microsc.*, **238** (2010) 57.
[13] Schröder-Turk G. E. *et al.*, *Adv. Mater.*, **23** (2011) 2535.
[14] Chiu S. N., Stoyan D., Kendall W. S. and Mecke J., *Stochastic Geometry and Its Applications* (Wiley, New York) 2013.
[15] Schröder-Turk G. E., Mickel W., Kapfer S. C., Schaller F. M., Breidenbach B., Hug D. and Mecke K., *New J. Phys.*, **15** (2013) 083028.
[16] Mecke K., Buchert T. and Wagner H., *Astron. Astrophys.*, **288** (1994) 697.
[17] Schmalzing J., Buchert T., Melott A. L., Sahni V., Sathyaprakash B. S. and Shandarin S. F., *Astrophys. J.*, **526** (1999) 568.
[18] Marinucci D., *Stat. Sci.*, **19** (2004) 294.
[19] Gay C., Pichon C. and Pogosyan D., *Phys. Rev. D*, **85** (2012) 023011.
[20] Ducout A., Bouchet F. R., Colombi S., Pogosyan D. and Prunet S., *Mon. Not. R. Astron. Soc.*, **429** (2013) 2104.
[21] Wiegand A., Buchert T. and Ostermann M., *Mon. Not. R. Astron. Soc.*, **443** (2014) 241.
[22] Wiegand A. and Eisenstein D. J., *Mon. Not. R. Astron. Soc.*, **467** (2017) 3361.
[23] Chingangbam P., Ganesan V., Yogendran K. P. and Park C., *Phys. Lett. B*, **771** (2017) 67.
[24] Pranav P., van de Weygaert R., Vegter G., Jones B. J. T., Adler R. J., Feldbrugge J., Park C.,

Buchert T. and Kerber M., *Mon. Not. R. Astron. Soc.*, **485** (2019) 4167.
[25] Sullivan J. M., Wiegand A. and Eisenstein D. J., *Mon. Not. R. Astron. Soc.*, **485** (2019) 1708.
[26] Armstrong R. T., McClure J. E., Robins V., Liu Z., Arns C. H., Schlüter S. and Berg S., *Transport Porous Media*, **130** (2018) 305.
[27] Herminghaus S., Jacobs K., Mecke K., Bischof J., Fery A., Ibn-Elhaj M. and Schlagowski S., *Science*, **282** (1998) 916.
[28] Spengler C., Nolle F., Mischo J., Faidt T., Grandthyll S., Thewes N., Koch M., Müller F., Bischoff M., Klatt M. A. and Jacobs K., *Nanoscale*, **11** (2019) 19713.
[29] Wittmann R., Sitta C. E., Smallenburg F. and Löwen H., *J. Chem. Phys.*, **147** (2017) 134908.
[30] Barbosa M., Natoli R., Valter K., Provis J. and Maddess T., *Biomed. Opt. Express*, **5** (2014) 2317.
[31] Barbosa M., Maddess T., Ahn S. and Chan-Ling T., *Sci. Rep.*, **9** (2019) 1.
[32] Räth C., Monetti R., Bauer J., Sidorenko I., Müller D., Matsuura M., Lochmüller E.-M., Zysset P. and Eckstein F., *New J. Phys.*, **10** (2008) 125010.
[33] Klatt M. A., Schröder-Turk G. E. and Mecke K., *Med. Phys.*, **44** (2017) 3663.
[34] Wang F. and Landau D. P., *Phys. Rev. Lett.*, **86** (2001) 2050.
[35] Aharonian F. *et al.*, *Science*, **307** (2005) 1938.
[36] Wang F. and Landau D. P., *Phys. Rev. E*, **64** (2001) 056101.
[37] Ebner B., Henze N., Klatt M. A. and Mecke K., *Electron. J. Statist.*, **12** (2018) 2873.
[38] Klatt M. A., *Morphometry of random spatial structures in physics*, PhD Thesis, Friedrich-Alexander-Universität Erlangen-Nürnberg (FAU) (2016).
[39] Cressie N. A. C., *Statistics for Spatial Data, Wiley Series in Probability and Mathematical Statistics* (Wiley, New York) 1993.
[40] Møller J. and Waagepetersen R. P., *Statistical Inference and Simulation for Spatial Point Processes* (Chapman & Hall, Boca Raton) 2003.
[41] Illian J., Penttinen A., Stoyan H. and Stoyan D., *Statistical Analysis and Modelling of Spatial Point Patterns* (John Wiley & Sons, Chichester) 2008.
[42] Svane A. M., *J. Math. Imaging Vis.*, **49** (2014) 352.
[43] Hug D., Kiderlen M. and Svane A. M., *Discrete Comput. Geom.*, **57** (2017) 545.
[44] Klatt M. A., *minkmaps–C++ code for a Morphometric Statistical Analysis via Minkowski Maps*, GitHub, `https://github.com/michael-klatt/minkmaps` (2019).
[45] Klatt M. A. and Mecke K., *Supplementary Dataset for Detecting Structured Sources in Noisy Images via Minkowski Maps*, *Zenodo*, `https://doi.org/10.5281/zenodo.3404001` (2019).
[46] H.E.S.S. Collaboration, *H.E.S.S. First Public Test Data Release*, `https://doi.org/10.5281/zenodo.1421098` (2018).